



## Article

# Comparison of VLF Signal Responses to Solar Flares along Daytime and Nighttime Propagation Paths

Xudong Gu <sup>1</sup>, Juan Yi <sup>1</sup>, Shiwei Wang <sup>1,\*</sup>, Zejun Hu <sup>2</sup>, Wei Xu <sup>1,3</sup>, Binbin Ni <sup>1,3</sup>, Bin Li <sup>2</sup>, Fang He <sup>2</sup>, Xiangcai Chen <sup>2</sup> and Hongqiao Hu <sup>2</sup>

<sup>1</sup> Department of Space Physics, School of Electronic Information, Wuhan University, Wuhan 430072, China

<sup>2</sup> MNR Key Laboratory for Polar Science, Polar Research Institute of China, Shanghai 200136, China

<sup>3</sup> Hubei Luoqia Laboratory, Wuhan 430072, China

\* Correspondence: wangsw@whu.edu.cn; Tel.: +86-177-2020-4837

**Abstract:** Solar flares have a severe impact on the near-earth space environment, during which the VLF signals observed by the ground-based instrument exhibit abnormal changes. However, the similarity and differences of VLF signal responses to solar flares over daytime and nighttime propagation paths are still unclear. Previous magnetograph measurements suggest that solar flares can also influence the dark hemisphere by the induction currents caused by the change in the ionospheric electrical conductivity of the sunlit hemisphere. To examine these effects, we have analyzed the solar flare effects on VLF propagation along two paths that are suited along the north–south direction, but with a time difference of 12 h. From late March to late May in the year of 2022, a total of 32 flare events with clear VLF responses are selected in order to analyze the similarity and differences between daytime and nighttime propagation paths. Different from the previous magnetograph measurements, it is found that the solar flare effects can only be observed from daytime VLF propagation paths. Moreover, present results show that the amplitude and phase variation of the VLF signal increases almost linearly with the magnitude of solar flares, and the stronger the solar flare, the more obvious the influence on VLF signals. However, the two paths exhibit notably different sensitivity in terms of amplitude and phase variation to solar flare class. Future studies that aim at nowcasting solar flare events using ground-based VLF receivers need to take these effects into account. The goal is to better understand the effects of solar flares on the lower ionosphere, with a view toward improving the nowcasting capability of the VLF technique for solar flares.

**Keywords:** VLF transmitter signal; solar flare; daytime path; nighttime path; VLF signal responses



**Citation:** Gu, X.; Yi, J.; Wang, S.; Hu, Z.; Xu, W.; Ni, B.; Li, B.; He, F.; Chen, X.; Hu, H. Comparison of VLF Signal Responses to Solar Flares along Daytime and Nighttime Propagation Paths. *Remote Sens.* **2023**, *15*, 1018. <https://doi.org/10.3390/rs15041018>

Academic Editor: Panagiotis Kosmopoulos

Received: 31 December 2022

Revised: 5 February 2023

Accepted: 10 February 2023

Published: 12 February 2023



**Copyright:** © 2023 by the authors. Licensee MDPI, Basel, Switzerland. This article is an open access article distributed under the terms and conditions of the Creative Commons Attribution (CC BY) license (<https://creativecommons.org/licenses/by/4.0/>).

## 1. Introduction

The solar flare is one of the most energetic processes in the solar system, which releases up to  $\sim 10^{25}$  J energy in tens of minutes, thereby causing instantaneous local heating and intense emission of electromagnetic energy and X-ray fluxes [1,2]. Solar flares can profoundly influence the spacecraft environment, radio communications, and navigation since it dramatically changes the near-earth space environment, including the D-region ionosphere at 60–90 km altitude [3,4]. Very-low-frequency (VLF, 3–30 kHz) waves, originating from both natural and artificial sources, can propagate within the earth-ionosphere waveguide (EIWG). In the classic waveguide mode theory, an infinite series of discrete waveguide modes are usually used to describe the propagation of VLF waves in a flat, infinitely wide waveguide with parallel, sharply defined boundaries, representing EIWG. Each waveguide mode can be found by superposing two plane waves, which reflect back and forth in this waveguide, propagating at a particular angle of incidence [5,6]. VLF signals are well bounded between the Earth's surface and the D-region ionosphere, and abnormal changes in VLF signals are mostly related to the disturbance of the lower ionosphere. Therefore, VLF signals have been widely used for submarine communication,

subionospheric remote sensing, geophysical exploration, and monitoring of space weather events [7]. The X-ray fluxes emitted by solar flares can cause an increase in ionization and, thus, enhancement of electron density in the D-region ionosphere. The lowering of the upper boundary of the earth-ionosphere waveguide significantly affects the propagation of VLF waves, manifested in amplitude and phase changes [8–15].

Solar flares have been long investigated using ground-based measurements of VLF signals from navy transmitters [16–18]. The statistical analysis shows that the flare-induced amplitude and phase change of VLF signals scales almost linearly with the logarithm of the X-ray flux, and the time of the amplitude peak for most events is 1–6 min later than that of the X-ray flux [19–21]. Based on this relation, the ground-based VLF detection system has been suggested to be capable of nowcasting the eruption and magnitude of solar flares [22,23]. Authors of Ref [24] analyzed the effects of solar flares on the amplitude and phase of VLF signals using measurements of VLF signals from the NSC (Niscemi, Sicily, Italy, 45.9 kHz) and ICV (Tavdara Island, Sardinia, Italy, 20.27 kHz) transmitters at the Belgrade Station for 200 flare events between 2008 and 2014. For two transmitters with different frequencies, the amplitude measurements of ICV signals were found to be more sensitive to the flare than the phase due to the sudden ionospheric disturbances. Conversely, the phase measurement was more sensitive than the amplitude for the NSC transmitter. The temporal evolution of VLF amplitude disturbance is similar to that of X-ray fluxes during solar flares. The simulation results using the long wave propagation capability (LWPC) model [25] are in good agreement with the observation results [26], indicating the close relationship between X-ray fluxes emitted by solar flares and the disturbance of electron density in the D-region ionosphere. More recent simulations show that the amplitude and phase of VLF signals during solar flares may increase or decrease depending on the distance between the transmitter and receiver for the reason that this distance affects the local modal composition of the VLF signals and then determine the sign of signal perturbation parameters [27].

Various studies have been devoted to generalizing the VLF response to solar flares, mainly using measurements of VLF transmitter signals collected along propagation paths that are partially or entirely under daytime conditions. It is well-expected that solar flares only affect the sunlit hemisphere. However, observational evidence from magnetograph measurements suggests that geomagnetic effects associated with solar flares can also influence the dark hemisphere, caused by a sudden increase in the electrical conductivity of the sunlit hemisphere, forcing the induced current to flow in the ionosphere to the dark side of the Earth [28,29]. Whether this process affects the propagation of VLF signals during solar flares for propagation paths under nighttime conditions is the main focus of this study.

More studies are needed to more precisely quantify the characteristics and differences of VLF responses to solar flares along the daytime and nighttime propagation paths. The sun has become more active during the first half of 2022, and numerous solar flare events, including a total of 6 X-class events, have occurred from late March to early May, providing an excellent opportunity to better understand the unsolved problems in solar flare studies. It is from this perspective that, in the present study, we analyze the similarity and difference in terms of VLF response between two propagation paths that are distributed almost along the north–south direction and have a time difference of 12 h. The goal is to better understand the effects of solar flares on the lower ionosphere, with a view toward improving the nowcasting capability of the VLF technique for solar flares.

## 2. Instrument and Database

In this study, for the sake of direct comparison, we purposely choose two VLF propagation paths to investigate the daytime and nighttime difference in VLF response to solar flares. For both paths, the transmitter and receiver are located almost along the same longitude line, and thus, the recorded VLF signal is less influenced by the effects of the solar zenith angle. As shown in Figure 1, the NAA transmitter, as marked using a red triangle, is

located in Cutler (44.64°N, 67.28°W) in the Maine state of the United States, operating at a frequency of 24 kHz, and the propagation of its signal to the Chinese Great Wall Station (GWS, 62.2°S, 58.96°W) in Antarctica is almost along the same longitudinal line. The NWC transmitter located in the North West Cape (24.81°S, 114.16°E) in Australia operates at a frequency of 19.8 kHz, and its transmitted signal can propagate along the same longitude line to the Suizhou station (SZS, 31.5°N, 113.32°E) in China. The distance between two neighboring pink dashed lines is 2000 km, and the green dashed lines show similar results, but for the SZS. The NAA-GWS path is about 12,000 km, while the NWC-SZS path is about 6000 km, which is about half of the NAA-GWS path. The Universal Time (UT) is determined based on the prime meridian at 0° longitude, and the local time is UT-4 and UT+8 for the NAA-GWS (60°W) and NWC-SZS (120°E) paths, respectively. Namely, the time difference between the NAA-GWS path and the NWC-SZS path is about 12 h. The local noon for the NAA-GWS path is almost the local midnight for the NWC-SZS path. Therefore, these two paths are ideally suited to examine if solar flares can influence VLF propagation in the dark hemisphere.

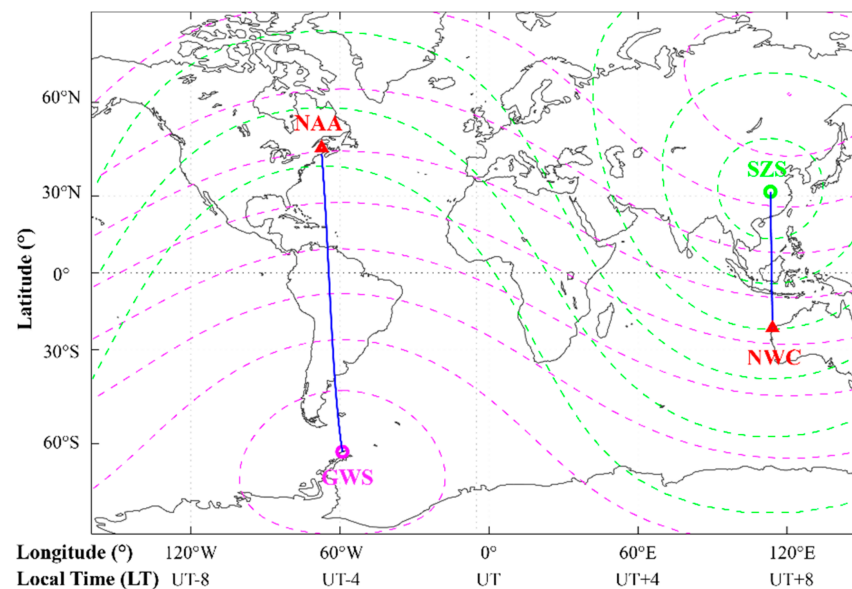


**Figure 1.** The propagation paths of the NAA signal to the GWS and the NWC signal to the SZS. The red triangles mark the transmitters, and the pink and green circles mark the receiving stations. The propagation path is illustrated using the blue line between the transmitter and receiving station. The pink dashed lines are the auxiliary line centered at GWS and separated by 2000 km, and the green dashed lines are the auxiliary line centered at SZS and separated by 2000 km.

### 2.1. The WHU ELF/VLF Instrument

The WHU ELF/VLF receiver, which is designed and developed by Wuhan University (WHU) for the reception of broadband ELF and VLF radio waves [30–32], has been deployed at the SZS and GWS stations. This instrument uses 16 bits analog to digital converter (ADC) with a 250 kHz sampling rate and can detect both natural and artificial ELF/VLF signals in the frequency range of 1–50 kHz. The VLF data recorded by this instrument have been widely utilized in studies related to the tweek atmospherics, the lightning location, and the sunrise effect of VLF transmitter signals [33–38]. The WHU ELF/VLF receiver comprises two orthogonal magnetic loop antennas, set up in both north–south (NS) and east–west (EW) directions, to record the broadband VLF data separately. The amplitude and phase of VLF signals are extracted using the minimum-shift keying (MSK) modulation method [21,39]. The two transmitter-receiver paths utilized in the present study are located along the south–north direction, and thus, the VLF data collected by the NS channel of our receivers have relatively lower background noise and better data quality. Only the amplitudes and phases of NS channels are investigated in this study.

## 2.2. The Criterion for Selecting Solar Flare Events and the Detrending Method

The magnitude of solar flares is determined based on the X-ray flux data provided by XRS-B (1–8 Å channel) measurement on the Geostationary Operational Environment Satellite (GOES) 16 and 17 satellites, as obtained from the National Oceanic and Atmospheric Administration (NOAA) website (available at <https://data.ngdc.noaa.gov/platforms/solar-space-observing-satellites/goes/>, accessed on 1 September 2022). An M-class solar flare corresponds to a peak X-ray flux of  $10^{-5} \text{ W/m}^{-2}$ , while an X-class corresponds to a peak flux of  $10^{-4} \text{ W/m}^{-2}$ . Because the WHU ELF/VLF receiver was deployed in Antarctica in the first quarter of 2022 and the main goal of this study is to investigate the solar flare events of the current solar cycle or within a relatively short time window, using the X-ray flux data collected from 25 March to 25 May 2022, a total of 65 M- and X-class solar flares are selected as candidate events in this study.

To unbiasedly analyze the VLF response to solar flares, the prerequisite conditions are listed below:

- (1) To minimize the sunrise and sunset effects [38,40], solar flares that occur half an hour before and after the local sunrise or sunset time are not considered. The sunrise or sunset time corresponding to the VLF propagation path is jointly determined by the local sunrise or sunset time at the transmitter and the receiving station. The local sunrise and sunset time are obtained from the NOAA Global Monitoring Laboratory (<https://gml.noaa.gov/grad/solcalc/>, accessed on 1 September 2022).
- (2) Moreover, for the sake of comparison, we only consider those flare events with high-quality VLF measurements with a signal-to-noise ratio (SNR) higher than 3 dB. VLF measurements with SNR lower than 3 dB in either NAA-GWS or NWC-SZS path are considered as low-quality and not used in the present study.

To unbiasedly analyze the flare effect, we mainly focus on the net change of VLF amplitude and phase in the present study. Typical VLF signals measured during quiet time conditions exhibit diurnal variations due to the change in solar input. To calculate the net effects of solar flares, a detrending method is first applied to remove the background trend of VLF data. First, we find out the duration ( $\Delta t$ ) of each solar flare event by subtracting the start time ( $t_1$ ) from the peak time ( $t_2$ ) based on the X-ray flux data. Then, we fit the X-ray flux data from  $t_1 - \Delta t$  to  $t_1$  (without the influence of solar flares) and find the flare-excluded X-ray flux ( $F_1$ ) at  $t_2$ . Finally, we calculated the flare-induced X-ray flux at  $t_1$  by subtracting  $F_1$  from the observed X-ray flux. With the same method, we can also find out the background trend of amplitude and phase measurements, and further calculate the net effects of VLF amplitude and phase driven by solar flare events, the amplitude change ( $\Delta_{\text{Amp}}$ ) and phase change ( $\Delta_{\text{Pha}}$ ).

## 3. Observations

We use two typical events to showcase the VLF response to solar flares for the daytime and nighttime propagation paths. Figure 2 shows the VLF measurements of NAA signals at GWS during an X-class flare event, as well as the measurements of NWC signals at SZS. The NAA-GWS path is under daytime conditions, while the NWC-SZS path is under nighttime conditions. The red line in Figure 2a indicates the variation of X-ray fluxes for the solar flare event that occurred on 30 March 2022. This solar flare event started at  $\sim 17:21$  UT ( $t_1$ ), and the X-ray flux increased rapidly from  $\sim 10^{-6} \text{ W/m}^{-2}$  to  $\sim 10^{-4} \text{ W/m}^{-2}$  at  $\sim 17:44$  UT with the peak at  $\sim 17:37$  UT ( $t_2$ ), which was an X1.3 solar flare. The received amplitude and phase of the NAA signal show slight variation until the X-ray flux begins to increase (Figure 2b,c). The amplitude and phase change, compared to pre-flare conditions, as caused by this flare event is  $\sim 7.36$  dB and  $\sim 279.61^\circ$ , respectively. VLF signal responded almost simultaneously to the increase of X-ray fluxes, and for this reason, VLF remote sensing technique has been utilized to nowcast solar flare events [20,21,24]. However, during the same time period, the NWC signals received at SZS were almost invariant during this flaring event. The mean value and standard deviation from  $t_1$  to  $t_2$  (between the two red dotted lines) are about  $-49.88$  and  $0.41$  dB, respectively, for the amplitude data (Figure 2d). These values

are approximately 5.13 and 3.65 degrees for the phase data (Figure 2e). Due to the heavy fluctuation of VLF measurements, it is impossible to find out the background trend of amplitude and phase measurements, and to further calculate the net effects caused by solar flares. However, it is evidenced in Figure 2d,e that both the amplitude and phase data measured from the nighttime propagation path fluctuated around the mean value, and we observe no clear effects, for example, the effects found for the daytime paths (Figure 2b,c). It is from this perspective that the  $\Delta_{\text{Amp}}$  and  $\Delta_{\text{Pha}}$  of these propagation paths are marked with “no response”. The possible reason is that the local time (LT) of the NAA and GWS is  $\sim 13:30$  LT, while this solar flare occurs at  $\sim 17:30$  UT. The NAA signal propagates to the receiver along the daytime path, while the NWC signal propagates to SZS at  $\sim 01:30$  LT along the nighttime path. The VLF responses to the same solar flare during the daytime and nighttime are obviously different, and amplitude and phase changes can only be observed in the daytime propagation path.

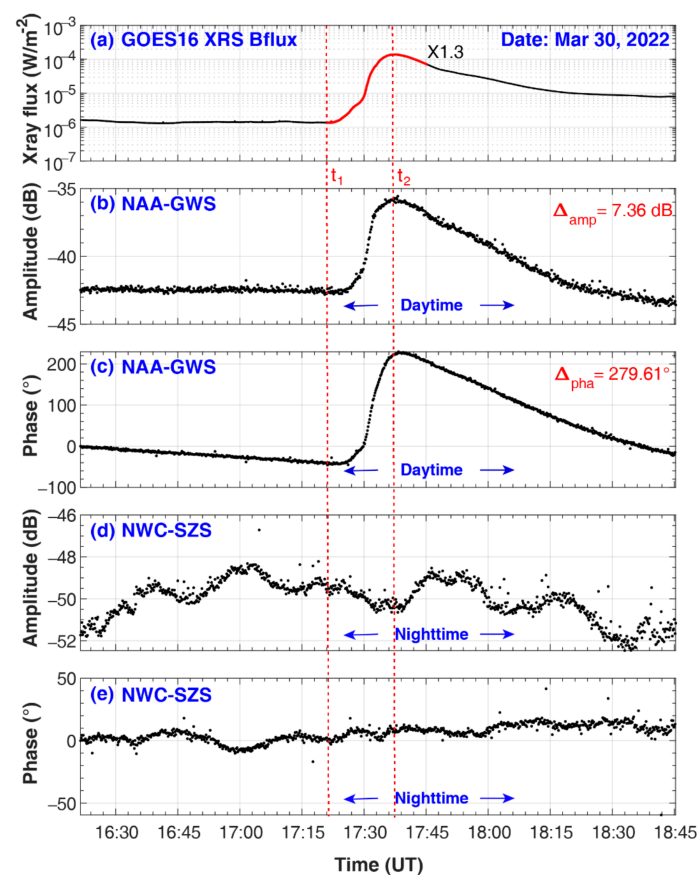


**Figure 2.** Responses of VLF signals to the X1.3 solar flare event on 30 March 2022, (a) the variation of X-ray flux, (b,c) the amplitude and phase of NAA signals observed at the GWS station, and (d,e) the amplitude and phase of NWC signals observed at the SZS station.

To further illustrate the difference between the daytime and nighttime propagation paths, the X1.1 class solar flare event, occurring at  $\sim 03:30$  UT on 17 April 2022, is also investigated in this study. Different from the first case, the NWC-SZS propagation path was under local daytime conditions when the solar flare occurred, while the NAA-GWS propagation path was under local nighttime conditions. As shown in Figure 3a, the X-ray flux gradually decreased until  $\sim 03:20$  UT and then increased from  $\sim 10^{-6}$   $\text{W}/\text{m}^{-2}$  to  $\sim 10^{-4}$   $\text{W}/\text{m}^{-2}$  during  $\sim 03:20$ – $03:35$  UT. As shown in Figure 3, the amplitude and phase of the NAA signal show little correlation with this solar flare, while those of the NWC signal have increased by  $\sim 1.34$  dB and  $\sim 127.06^\circ$ , respectively. This X-class solar flare occurred from  $\sim 11:20$  to  $\sim 11:35$  LT in the NWC-SZS path and from  $\sim 23:20$  to  $23:35$  LT in the NAA-GWS

path. We have only observed a clear change in VLF transmitter signals for the NWC-SZS path. This proves that the solar flare only influences the daytime propagation path and has little or no impact on the nighttime propagation path.

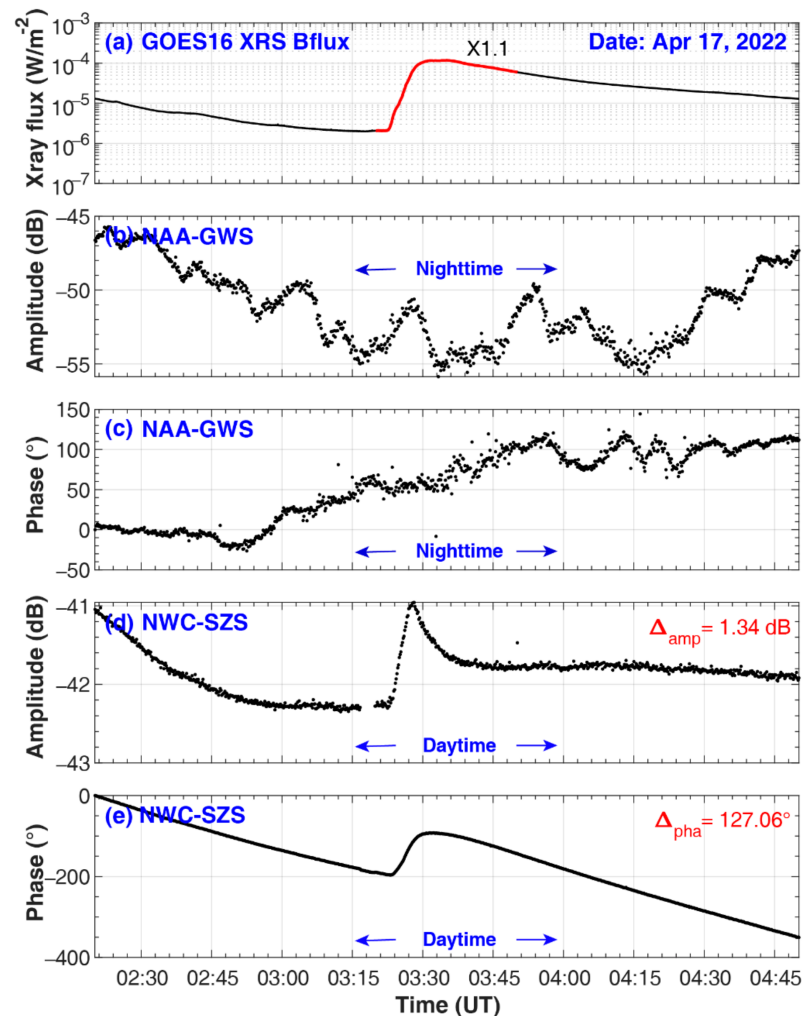


Figure 3. Same as Figure 2, except for the solar flare occurred on 17 April 2022.

Moreover, we use the VLF measurements from March to May in 2022 to reveal what effects M- and X-class solar flares have on VLF signals over the daytime and nighttime path as an attempt to give a general picture of the solar flare effects. According to the selection criteria listed in Section 2.2, from 25 March to 25 May 2022, a total of 32 flare events with high-quality VLF measurements are utilized in the present study. The detailed information of each event is summarized in Table 1, which lists the number, start time, peak time, end time, class, X-ray flux, and the  $\Delta_{\text{Amp}}$  and  $\Delta_{\text{Pha}}$ . Table 1 lists 5 X-class solar flares and 27 M-class solar flares; “no response” refers to those cases in which no clear VLF response is observed. The  $\Delta_{\text{Amp}}$  and  $\Delta_{\text{Pha}}$  are determined by the differences between the peak amplitude/phase and the initial amplitude/phase during the solar flare period. To only focus on the net effect driven by the solar flare event, the peak amplitude/phase is calculated based on the detrending method, which is aimed to remove the regular variation trend for the quiet time. Note that  $\Delta_{\text{Pha}}$  was mostly found to be positive during solar flare events for propagation paths longer than 4000 km [27,41] and if the  $\Delta_{\text{Pha}}$  is positive is largely dependent on the location of VLF measurements. The solar flares, inducing the response of the NWC signals and having no significant effect on the NAA signals (represented by the black records), tend to occur during 00:00–08:00 UT, which is 08:00–16:00 LT along the NWC-SZS path. The rows highlighted in blue show those cases in that only the NAA signals

responded to the solar flare events. These events generally occurred during 12:00–20:00 UT, which is 08:00–16:00 LT for the NAA-GWS path. It is worth noting that among all the selected events, we found no event in which both the NWC-SZS and NAA-GWS paths responded to the same solar flare event. The responses of the VLF signal to solar flares along the NAA-GWS and NWC-SZS propagation paths show that solar flares only affect the VLF signal in the daytime path, but have no obvious impact on the nighttime path.

**Table 1.** List of the solar flare events and the corresponding responses of NAA and NWC transmitter signals during the period from 25 March 2022 to 25 May 2022.

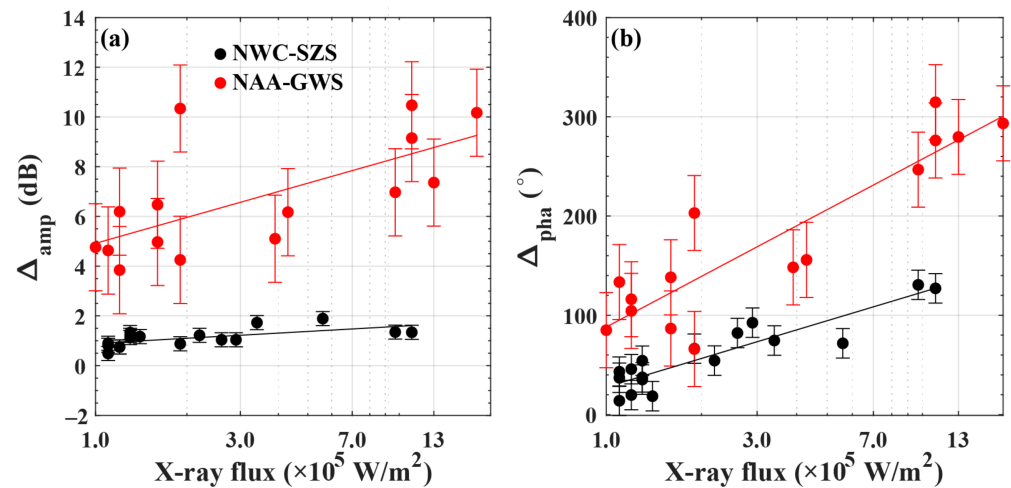
#	Start Time (UT)	Peak Time (UT)	End Time (UT)	Class	X-ray Flux ( $\times 10^{-5} \text{ W}\cdot\text{m}^2$ )	NWC-SZS		NAA-GWS	
						$\Delta_{\text{Amp}}$ (dB)	$\Delta_{\text{Pha}}$ ( $^{\circ}$ )	$\Delta_{\text{Amp}}$ (dB)	$\Delta_{\text{Pha}}$ ( $^{\circ}$ )
1	2022-03-29 00:59:34	2022-03-29 01:12:02	2022-03-29 01:24:53	M2.2	2.2	1.22	54.33	No response	No response
2	2022-03-29 01:52:17	2022-03-29 01:58:12	2022-03-29 02:02:13	M1.1	1.1	0.49	13.94	No response	No response
3	2022-03-30 17:21:28	2022-03-30 17:37:40	2022-03-30 17:45:19	X1.3	13	No response	No response	7.36	279.61
4	2022-03-31 18:21:15	2022-03-31 18:35:06	2022-03-31 18:44:11	M9.7	9.7	No response	No response	6.97	246.71
5	2022-04-02 02:42:05	2022-04-02 02:56:41	2022-04-02 03:05:30	M2.9	2.9	1.04	92.48	No response	No response
6	2022-04-02 13:21:42	2022-04-02 13:55:39	2022-04-02 14:39:21	M3.9	3.9	No response	No response	5.10	148.21
7	2022-04-02 17:37:58	2022-04-02 17:44:53	2022-04-02 17:49:59	M4.3	4.3	No response	No response	6.17	155.72
8	2022-04-15 13:50:07	2022-04-15 13:59:16	2022-04-15 14:09:52	M1.9	1.9	No response	No response	4.25	65.99
9	2022-04-16 14:48:48	2022-04-16 14:56:26	2022-04-16 15:08:21	M1.0	1.0	No response	No response	4.76	85.01
10	2022-04-17 01:29:07	2022-04-17 02:11:20	2022-04-17 02:25:26	M1.9	1.9	0.88	66.38	No response	No response
11	2022-04-17 03:20:08	2022-04-17 03:35:04	2022-04-17 03:50:11	X1.1	11	1.34	127.06	No response	No response
12	2022-04-17 19:55:37	2022-04-17 20:02:32	2022-04-17 20:05:08	M1.6	1.6	No response	No response	6.47	86.64
13	2022-04-18 07:41:05	2022-04-18 07:48:43	2022-04-18 07:52:27	M1.3	1.3	1.22	37.47	No response	No response
14	2022-04-19 04:43:14	2022-04-19 04:50:31	2022-04-19 04:58:17	M1.1	1.1	0.82	43.19	No response	No response
15	2022-04-20 12:28:01	2022-04-20 12:53:46	2022-04-20 13:00:38	M1.9	1.9	No response	No response	10.34	202.96
16	2022-04-21 01:49:38	2022-04-21 01:59:23	2022-04-21 02:03:55	M9.7	9.7	1.35	130.61	No response	No response
17	2022-04-22 04:55:21	2022-04-22 05:14:37	2022-04-22 05:27:10	M1.1	1.1	0.90	37.07	No response	No response
18	2022-04-25 01:23:57	2022-04-25 02:00:53	2022-04-25 02:35:37	M1.3	1.3	1.13	54.28	No response	No response
19	2022-04-25 03:56:17	2022-04-25 04:02:18	2022-04-25 04:05:52	M1.2	1.2	0.75	45.75	No response	No response

Table 1. Cont.

#	Start Time (UT)	Peak Time (UT)	End Time (UT)	Class	X-ray Flux ( $\times 10^{-5} \text{ W}\cdot\text{m}^2$ )	NWC-SZS		NAA-GWS	
						$\Delta_{\text{Amp}}$ (dB)	$\Delta_{\text{Pha}}$ ( $^{\circ}$ )	$\Delta_{\text{Amp}}$ (dB)	$\Delta_{\text{Pha}}$ ( $^{\circ}$ )
20	2022-04-29 07:16:34	2022-04-29 07:30:19	2022-04-29 07:41:26	M1.2	1.2	0.75	19.69	No response	No response
21	2022-04-29 18:01:27	2022-04-29 18:09:56	2022-04-29 18:20:59	M1.2	1.2	No response	No response	3.84	116.12
22	2022-04-30 04:49:48	2022-04-30 05:01:11	2022-04-30 05:05:35	M2.6	2.6	1.04	82.14	No response	No response
23	2022-04-30 05:25:28	2022-04-30 05:35:01	2022-04-30 05:39:19	M1.4	1.4	1.17	18.52	No response	No response
24	2022-04-30 13:39:26	2022-04-30 13:47:44	2022-04-30 13:51:17	X1.1	11	No response	No response	9.15	314.62
25	2022-05-03 07:39:02	2022-05-03 07:53:57	2022-05-03 08:00:13	M1.3	1.3	1.33	35.31	No response	No response
26	2022-05-03 13:17:07	2022-05-03 13:25:36	2022-05-03 13:30:12	X1.1	11	No response	No response	10.47	276.12
27	2022-05-04 16:07:29	2022-05-04 16:32:41	2022-05-04 16:55:51	M1.2	1.2	No response	No response	6.19	104.36
28	2022-05-10 13:27:50	2022-05-10 13:55:51	2022-05-10 13:57:29	X1.8	18	No response	No response	10.17	293.30
29	2022-05-11 16:38:39	2022-05-11 16:49:43	2022-05-11 16:57:24	M1.6	1.6	No response	No response	4.97	138.22
30	2022-05-19 07:00:50	2022-05-19 07:19:12	2022-05-19 07:29:50	M5.6	5.6	1.89	71.75	No response	No response
31	2022-05-19 15:06:39	2022-05-19 15:16:06	2022-05-19 15:22:17	M1.1	1.1	No response	No response	4.63	133.39
32	2022-05-20 07:39:41	2022-05-20 07:45:07	2022-05-20 07:46:43	M3.4	3.4	1.73	74.55	No response	No response

This study further examines the relationship between the VLF response and the magnitude of solar flares at GWS and SZS, respectively. As shown in Figure 4, the  $x$ -axis represents the log-10-based X-ray fluxes corresponding to the different solar flare classes listed in Table 1 for all solar flare events. The red and black dots indicate the changes in amplitude (Figure 4a) and phase (Figure 4b) of the NAA and NWC signals, respectively. For both amplitude and phase variations, error bars show the uncertainty of each data point relative to the best-fit line [42]. For the NAA signals, the amplitude change caused by the  $\sim$ M1.0 solar flare is  $\sim$ 5 dB, while it is  $\sim$ 8.5 dB for an X1.0 flare event. On the other hand, the phase change is  $\sim$ 80 $^{\circ}$  and 250 $^{\circ}$  for the M1.0 and X1.0 flare events, respectively. The amplitude and phase perturbation of the VLF signal increase with the magnitude of solar flares, and a more-intense solar flare has a more obvious influence on the propagation of VLF signals. For solar flares with the same magnitude, the responses of the NAA transmitter signals are stronger than the NWC signals. The relation between amplitude change and logarithm-based X-ray fluxes can be best fitted using linear functions. We assume a simple function  $\Delta_{\text{Amp}} = A \log_{10}(\text{flux}) + B$  to approximate the amplitude and phase change produced by solar flares, similar to that used in [22,23]. Based on the uncertainty of each point, the uncertainties in the two parameters of the best-fit line can be evaluated. The best-fit functions that we found for the amplitude variation are  $\Delta_{\text{Amp}} = (1.57 \pm 0.65)\log_{10}(\text{flux}) + (6.72 \pm 0.09)$  and  $\Delta_{\text{Amp}} = (0.23 \pm 0.10)\log_{10}(\text{flux}) + (1.12 \pm 0.02)$  for the NAA-GWS and NWC-SZS path, respectively. The slope of amplitude variation of the NAA signals is about seven times larger than that of the NWC signals, which indicates that the NAA signal is more sensitive to solar

flare than the NWC signals. As for the phase measurements, the best-fit linear functions are  $\Delta_{\text{pha}} = (77 \pm 14)\log_{10}(\text{flux}) + (176.5 \pm 1.8)$  and  $\Delta_{\text{pha}} = (31.4 \pm 5.1)\log_{10}(\text{flux}) + (59.1 \pm 1.2)$ , respectively. The fitted results indicate the increases in the NAA signals are more pronounced than those of the NWC signals. The VLF signal disturbance is linearly correlated with the solar flare magnitude, expressed as the logarithm of the X-ray flux, which is consistent with previous studies [21,22].



**Figure 4.** The amplitude and phase variation versus the X-ray fluxes caused by the solar flare class, as well as fitting functions for the VLF signals (black for NWC-SZS and red for NAA-GWS).

#### 4. Discussions

Generally, the angle of incidence of the sunlight is closely related to local time (LT). At sunrise, the angle of incidence is about  $\sim 90^\circ$ , corresponding to the horizontal sunlight, gradually decreasing to  $0^\circ$  at noon, and then gradually increasing to  $90^\circ$  in the afternoon. The intensity of solar radiation is described using the cosine of the incidence angle [43,44]. As the incidence angle decreases, the intensity increases, and the energy released by the sun at noon, which reaches the Earth's atmosphere, is the largest, due to the fact that sunlight is almost perpendicular to the ground. Therefore, the local time dependence of VLF signal responses at GWS and SZS to solar flares is also analyzed in detail. The local time distribution of VLF signal amplitude and phase perturbations is shown in Figure 5. For solar flare events of magnitude less than  $\sim M3.0$ , the amplitude (Figure 5a) and phase (Figure 5b) perturbations of the NAA signal along the NAA-GWS propagation path show maximum values around 12:00 LT, except for individual data contaminated by more than one solar flare events, which are marked using red boxes. These points correspond to those solar flare events that occur within a short time window and overlap with each other. For these events, the net effects of solar flares cannot be distinguished from each other and cannot be extracted by the above-mentioned detrending method. We emphasize that these events are not used in the present study only because we cannot determine the net effects of each solar flare event. These trends (dashed red arrows) are roughly consistent with the above-mentioned variation of solar radiation versus LT, indicating that the solar incident angle may be a dominant parameter in the perturbation process of VLF signal by flares. However, for stronger solar flares, the response of the VLF signal to solar flares has no obvious correlation with LT, which may be involved in more complex physical processes. The NWC signal propagating along the NWC-SZS path shows a weaker regularity in response to solar flares than that for the NAA signal on the whole. However, after removing some outliers (marked by red boxes), similar regularity can still be seen in Figure 5c,d. In the future, more observations of solar flares are needed in order to clarify further the dependence of the VLF signal on the response of solar flares on LT. The development and application of a series of new physical models of energy transfer

from the sun to the Earth are needed to explain the physical processes that these response features undergo.

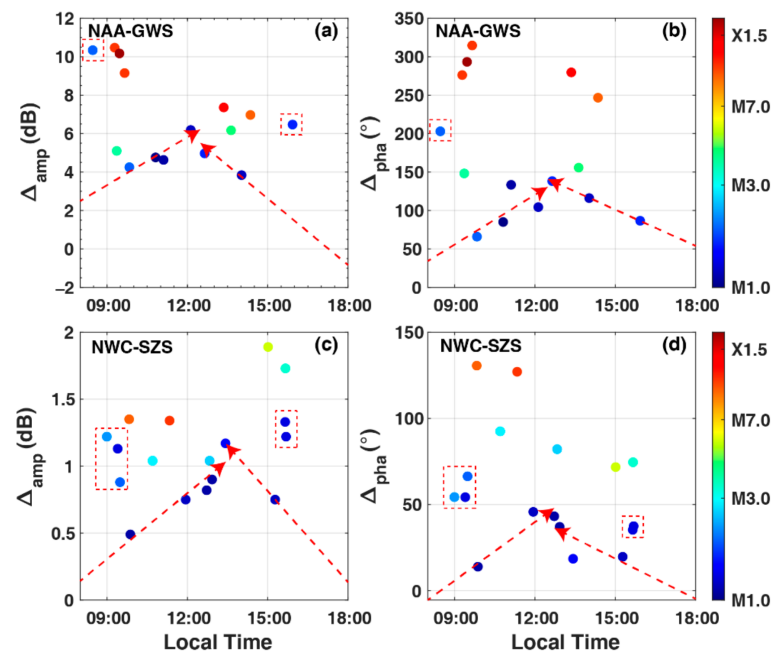


**Figure 5.** The VLF signal amplitude and phase perturbations to the solar flares as a function of local time for NWC and NAA transmitter signals, respectively.

Although magnetometer observations suggest that the solar flare effects do occur in the dark hemisphere [28,29], our observations show that clear VLF response to the solar flares can only be observed for the daytime propagation path. This indicates that Oshiro's theory is not suitable to explain the effects of solar flares on VLF signals, and the physical mechanism behind the geomagnetic disturbance and VLF signal disturbance, although both caused by solar flares, is different. Solar flares occurring in the Earth's sunlit hemisphere can alter the ionospheric electron density, as well as the Earth's magnetic field [45]. Singh et al. [16] evaluated the reflection height ( $H'$ ) and the sharpness factor ( $\beta$ ) of the D region ionosphere, and the result shows that the  $H'$  decreases while the  $\beta$  increases with the increase of the solar flare power due to the increased ionization caused by the solar flare events. The  $H'$  is higher and the  $\beta$  smaller at low latitudes than those at mid and high latitudes. Selvakumaran's work [17] shows that the local time dependence of solar flare effects can change the VLF amplitude and time delay between VLF peak amplitude and X-ray flux peak, and the local time of flare's occurrence and their classes strongly affect the  $H'$  and  $\beta$ , which can be used to estimate the flare time electron density. The electron density increases exponentially with an increase in the solar flux intensity, and the solar flare effect can affect the horizontal component of the Earth's magnetic field due to the additional magnetic field produced by the ionospheric electrojet over the equatorial station. Rathore et al. [18] found that during the solar flare period, the X-ray flux enhancement can cause the sudden enhancement of D-region ionization and then the enhancement of VLF signal amplitude. Oshiro's work shows that solar flares can disrupt the electrical current system around the Earth, which is transported into the nightside and therefore affects the nightside magnetic field. The fact that no significant effect on the VLF signal has been found for the nighttime propagation paths indicates that the change in ionospheric current on the nightside caused by solar flares does not influence the propagation of the VLF signals. In this paper, two VLF propagation paths along the same longitude line are utilized, and these two paths are either under daytime or nighttime conditions. However, the VLF signal also shows a certain degree of disturbance when part of the propagation path is under daytime, that is, the mixed day-night path [22]. Present results show that

solar flares influence the VLF signal propagation path partially or entirely located in the daytime. In addition, the electron concentration in the D region can also be calculated using the solar flare magnitude, but this is not the primary goal of the present work and will be investigated in our next-step work.

## 5. Conclusions

Solar flares can severely influence the near-earth space environment, during which the VLF signals observed by the ground-based instrument may have abnormal changes. However, the characteristics and differences of VLF responses to solar flares over daytime and nighttime propagation paths are still unclear. The enhanced solar activity between March and May 2022, with numerous M- and X-class solar flare events, provides an excellent opportunity for this study. Supported by the Chinese Meridian Project II, a WHU ELF/VLF wave detection system was set up in March 2022 at the GWS station in Antarctica. Based on the observations at GWS and SZS, the response characteristics of NAA and NWC signals to solar flares are analyzed using two VLF propagation paths distributed roughly along the north–south direction, NAA-GWS and NWC-SZS, with a time difference of about 12 h.

From 25 March 2022 to 25 May 2022, a total of 32 flare events with high-quality VLF measurements are selected to investigate the response characteristics of VLF signals over the daytime and nighttime propagation paths to solar flares. We find that the VLF responses to the same solar flare during the daytime and nighttime are obviously different, and a clear VLF response can only be observed in the daytime propagation path. As mentioned in the Section 4, the solar flares occurring on the dayside can change the ionospheric electrical conductivity. The corresponding induction currents are forced to travel to the far side of the Earth, affecting the low ionosphere at night. However, our measurements demonstrate that these effects are insignificant for the propagation of VLF signals in the EIWG. The amplitude and phase perturbation of the VLF signal increase with the magnitude of solar flares, roughly with a linear relation, and a stronger solar flare has a more obvious influence on VLF signals. However, there are significant differences in the sensitivity of amplitude and phase perturbations to solar flare class for different VLF propagation paths. It is conceivable that the sensitivity of each propagation path is controlled not only by solar flares but also by the ground conductivity and zenith angles. The previously reported studies revealed that the amplitude perturbation of different VLF signals for solar flare events depends on the frequency due to the effect of the second-order TM mode [14], and for the same solar flare event, the higher the frequency, the greater the amplitude perturbation would be [46]. Additionally, for the VLF propagation paths, the specific solar zenith angles can also affect the level of amplitude perturbation [46]. Future studies aiming at improving the nowcasting capability of the VLF technique for solar flares need to consider this effect.

**Author Contributions:** Data curation, X.G., Z.H. and F.H.; methodology, X.G., S.W., W.X. and J.Y.; validation, X.G., S.W. and Z.H.; investigation, X.G. and J.Y.; writing—original draft preparation, X.G. and J.Y.; writing—review and editing, X.G., W.X., Z.H., X.C., B.L. and H.H.; project administration, X.G. and B.N.; funding acquisition, X.G., B.N., W.X. and Z.H. All authors have read and agreed to the published version of the manuscript.

**Funding:** This work was supported by the National Natural Science Foundation of China (Grant Nos. 42188101, 42025404, 41874195, 42274205), the National Key R&D Program of China (Grant No. 2022YFF0503700), the B-type Strategic Priority Program of the Chinese Academy of Sciences (Grant No. XDB41000000), the Pre-research projects on Civil Aerospace Technologies (Grant Nos. D020308, D020104, D020303), and the open fund of Hubei Luojia Laboratory (Grant No. 220100051).

**Data Availability Statement:** The data presented in this study are available on request from the authors (X.G., guxudong@whu.edu.cn; S.W., wangsw@whu.edu.cn). The data are not publicly available due to institutional restrictions.

**Acknowledgments:** We are grateful to the editor, and anonymous reviewers for their assistance in evaluating this paper, the Chinese Meridian Project II, the Chinese National Antarctic Research Expedition for the support to the VLF wave detection program at GWS, and the 985 funded project of School of Electronic information, Wuhan University.

**Conflicts of Interest:** The authors declare no conflict of interest.

## References

- Fletcher, L.; Dennis, B.R.; Hudson, H.S.; Krucker, S.; Phillips, K.; Veronig, A.; Battaglia, M.; Bone, L.; Caspi, A.; Chen, Q.; et al. An observational overview of solar flares. *Space Sci. Rev.* **2011**, *159*, 19.
- Qian, L.; Wang, W.; Burns, A.G.; Chamberlin, P.C.; Solomon, S.C. Responses of the thermosphere and ionosphere system to concurrent solar flares and geomagnetic storms. *J. Geophys. Res. Space Phys.* **2020**, *125*, e2019JA027431. [[CrossRef](#)]
- Xiong, B.; Wan, W.; Liu, L.; Withers, P.; Zhao, B.; Ning, B.; Wei, Y.; Le, H.; Ren, Z.; Chen, Y.; et al. Ionospheric response to the x-class solar flare on 7 September 2005. *J. Geophys. Res. Space Phys.* **2011**, *116*, A11317. [[CrossRef](#)]
- Emslie, A.; Dennis, B.; Shih, A.; Chamberlin, P.; Mewaldt, R.; Moore, C.; Welsch, B. Global energetics of thirty-eight large solar eruptive events. *Astrophys. J.* **2012**, *759*, 71. [[CrossRef](#)]
- Poulsen, W.; Inan, U.; Bell, T. A multiple-mode three-dimensional model of VLF propagation in the Earth-ionosphere waveguide in the presence of localized D region disturbances. *J. Geophys. Res. Space Phys.* **1993**, *98*, 1705–1717. [[CrossRef](#)]
- Palit, S.; Raulin, J.-P.; Szpigel, S. Response of Earth's Upper Atmosphere and VLF Propagation to Celestial X-Ray Ionization: Investigation With Monte Carlo Simulation and Long Wave Propagation Capability code. *J. Geophys. Res. Space Phys.* **2018**, *123*, 10224–10238. [[CrossRef](#)]
- Cohen, M.B.; Inan, U.S.; Paschal, E.P. Sensitive broadband ELF/VLF radio reception with the AWESOME instrument. *IEEE Trans. Geosci. Remote Sens.* **2010**, *48*, 3–17. [[CrossRef](#)]
- Wait, J.R. Mode conversion and refraction effects in the Earth-ionosphere waveguide for VLF radio waves. *J. Geophys. Res. Space Phys.* **1968**, *73*, 5809. [[CrossRef](#)]
- Cummer, S.A.; Inan, U.S.; Bell, T.F. Ionospheric D region remote sensing using vlf radio atmospherics. *Radio Sci.* **1998**, *33*, 1781–1792. [[CrossRef](#)]
- Thomson, N.R.; Clilverd, A.M. Solar flare induced ionospheric D-region enhancements from VLF amplitude observations. *J. Atmos. Sol.-Terr. Phys.* **2001**, *63*, 1729–1737. [[CrossRef](#)]
- Žigman, V.; Grubor, D.; Šulić, D. D-region electron density evaluated from vlf amplitude time delay during x-ray solar flares. *J. Atmos. Sol.-Terr. Phys.* **2007**, *69*, 775–792. [[CrossRef](#)]
- Inan, U.S.; Cummer, S.A.; Marshall, R.A. A survey of ELF and VLF research on lightning-ionosphere interactions and causative discharges. *J. Geophys. Res. Space Phys.* **2010**, *115*, A00E36. [[CrossRef](#)]
- Thomson, N.R. Daytime tropical D region parameters from short path VLF phase and amplitude. *J. Geophys. Res. Space Phys.* **2010**, *115*, A09313. [[CrossRef](#)]
- Thomson, N.R.; Rodger, C.J.; Clilverd, M.A. Daytime D region parameters from long-path VLF phase and amplitude. *J. Geophys. Res. Space Phys.* **2011**, *116*, A11305. [[CrossRef](#)]
- Xu, W.; Marshall, R.A.; Bortnik, J.; Bonnell, J.W. An electron density model of the d-and e-region ionosphere for transionospheric vlf propagation. *J. Geophys. Res. Space Phys.* **2021**, *126*, e2021JA029288. [[CrossRef](#)]
- Singh, A.K.; Singh, A.K.; Singh, R.; Singh, R.P. Solar flare induced D-region ionospheric perturbations evaluated from VLF measurements. *Astrophys. Space Sci.* **2014**, *350*, 1–9. [[CrossRef](#)]
- Selvakumaran, R.; Maurya, A.K.; Gokani, S.A.; Veenadhari, B.; Kumar, S.; Venkatesham, K.; Phanikumar, D.V.; Singh, A.K.; Singh, D.; Singh, R. Solar flares induced D-region ionospheric and geomagnetic perturbations. *J. Atmos. Sol.-Terr. Phys.* **2015**, *123*, 102–112. [[CrossRef](#)]
- Rathore, V.S.; Kumar, S.; Singh, A.K.; Singh, A.K. Ionospheric response to an intense solar flare in equatorial and low latitude region. *Indian J. Phys.* **2018**, *92*, 1213–1222. [[CrossRef](#)]
- McRae, W.M.; Thomson, N.R. Solar flare induced ionospheric d-region enhancements from vlf phase and amplitude observations. *J. Atmos. Sol.-Terr. Phys.* **2004**, *66*, 77–87. [[CrossRef](#)]
- Tan, L.M.; Thu, N.N.; Ha, T.Q. Observation of the effects of solar flares on the NWC signal using the new VLF receiver at tay nguyen university. *Sun Geosph.* **2014**, *8*, 27–31.
- Gu, X.; Luo, F.; Peng, R.; Li, G.; Chen, H.; Wang, S.; Yi, J.; Li, Z.; Ni, B.; Zhao, Z.; et al. Response characteristics of very low frequency signals from JJI transmitter to solar flare events. *Chin. J. Geophys.* **2021**, *64*, 1508–1517. (In Chinese)
- George, H.E.; Rodger, C.J.; Clilverd, M.A.; Cresswell-Moorcock, K.; Brundell, J.B.; Thomson, N.R. Developing a Nowcasting Capability for X-Class Solar Flares Using VLF Radiowave Propagation Changes. *Space Weather.* **2019**, *17*, 1783–1799. [[CrossRef](#)]
- Belcher, S.R.G.; Clilverd, M.A.; Rodger, C.J.; Cook, S.; Thomson, N.R.; Brundell, J.B.; Raita, T. Solar flare X-ray impacts on long subionospheric VLF paths. *Space Weather.* **2021**, *19*, e2021SW002820. [[CrossRef](#)]
- Šulić, D.M.; Srećković, V.A. A comparative study of measured amplitude and phase perturbations of VLF and LF radio signals induced by solar flares. *Serb. Astron. J.* **2014**, *188*, 45–54. [[CrossRef](#)]
- Ferguson, J.A. Ionospheric model validation at VLF and LF. *Radio Sci.* **1995**, *30*, 775–782. [[CrossRef](#)]

26. Palit, S.; Basak, T.; Pal, S.; Mondal, S.K.; Chakrabarti, S.K. Effect of solar flares on ionospheric VLF radio wave propagation, modeling with GEANT4 and LWPC and determination of effective reflection height. In Proceedings of the 2014 XXXIth URSI General Assembly and Scientific Symposium (URSI GASS), Beijing, China, 16–23 August 2014; pp. 1–4.
27. Boudierba, Y.; NaitAmor, S.; Tribeche, M. Study of the solar flares effect on VLF radio signal propagating along NRK-ALG path using LWPC code. *J. Geophys. Res. Space Phys.* **2016**, *121*, 6799–6807. [[CrossRef](#)]
28. Ohshio, M. Solar flare effect on geomagnetic variation. *Rept. Ionos. Space Res. Jpn.* **1964**, *11*, 377–491.
29. Sastri, J.H.; Murthy, B.S. Geomagnetic effects in the dark hemisphere associated with solar flares. *J. Geomag. Geoelectr.* **1975**, *27*, 67–73. [[CrossRef](#)]
30. Chen, Y.; Yang, G.; Ni, B.; Zhao, Z.; Gu, X.; Chen, Z.; Wang, F. Development of ground-based ELF/VLF receiver system in Wuhan and its first results. *Adv. Space Res.* **2016**, *57*, 1871–1880. [[CrossRef](#)]
31. Chen, Y.; Ni, B.; Gu, X.; Zhao, Z.; Yang, G.; Zhou, C.; Zhang, Y. First observations of low latitude whistlers using WHU ELF/VLF receiver system. *Sci. China Tech. Sci.* **2017**, *60*, 166–174. [[CrossRef](#)]
32. Gu, X.; Wang, Q.; Ni, B.; Xu, W.; Wang, S.; Yi, J.; Hu, Z.; Li, B.; He, F.; Chen, X.; et al. First results of the wave measurements by the WHU VLF wave detection system at the Chinese Great Wall station in Antarctica. *J. Geophys. Res. Space Phys.* **2022**, *127*, e2022JA030784. [[CrossRef](#)]
33. Yi, J.; Gu, X.; Li, Z.; Lin, R.; Cai, Y.; Chen, L.; Ni, B.; Yue, X. Modeling and analysis of NWC signal propagation amplitude based on LWPC and IRI models. *Chin. J. Geophys.* **2019**, *62*, 3223–3234. (In Chinese)
34. Yi, J.; Gu, X.; Cheng, W.; Tang, X.; Chen, L.; Ni, B.; Zhou, R.; Zhao, Z.; Wang, Q.; Zhou, L. A detailed investigation of low latitude tweek atmospherics observed by the WHU ELF/VLF receiver: 2. Occurrence features and associated ionospheric parameters. *Earth Planet Phys.* **2020**, *4*, 238–245. [[CrossRef](#)]
35. Zhou, R.; Gu, X.; Yang, K.; Li, G.; Ni, B.; Yi, J.; Chen, L.; Zhao, F.; Zhao, Z.; Wang, Q.; et al. A detailed investigation of low latitude tweek atmospherics observed by the WHU ELF/VLF receiver: I. Automatic detection and analysis method. *Earth Planet Phys.* **2020**, *4*, 120–130. [[CrossRef](#)]
36. Gu, X.; Li, G.; Pang, H.; Wang, S.; Ni, B.; Luo, F.; Peng, R.; Chen, L. Statistical analysis of very low frequency atmospheric noise caused by the global lightning using ground-based observations in China. *J. Geophys. Res. Space Phys.* **2021**, *126*, e2020JA029101. [[CrossRef](#)]
37. Gu, X.; Chen, H.; Wang, S.; Lu, Z.; Ni, B.; Li, G.; Cheng, W. Extraction of Alpha transmitter signals from single-station observations using the direction-finding method. *Sci. China Tech. Sci.* **2022**, *65*, 1727–1737. [[CrossRef](#)]
38. Wang, S.; Ni, B.; Gu, X.; Lin, R.; Li, G.; Luo, F.; Peng, R.; Chen, H. Sunrise effect of Very-Low-Frequency JJJ transmitter signal propagation over an east-west path. *Chin. J. Geophys.* **2022**, *65*, 145–156. (In Chinese)
39. Gu, X.; Peng, R.; Wang, S.; Ni, B.; Luo, F.; Li, G.; Li, Z. Responses of the very low frequency transmitter signals during the solar eclipse on 26 December, 2019 over a North-South propagation path. *IEEE Trans. Geosci. Remote Sens.* **2022**, *60*, 2000207. [[CrossRef](#)]
40. Wang, S.; Gu, X.; Luo, F.; Peng, R.; Chen, H.; Li, G.; Ni, B.; Zhao, Z.; Yuan, D. Observations and analyses of the sunrise effect for NWC VLF transmitter signals. *Chin. J. Geophys.* **2020**, *63*, 4300–4311. (In Chinese)
41. Raulin, J.-P.; Trotter, G.; Kretschmar, M.; Macotela, E.; Pacini, A.; Bertoni, F.; Dammash, I. Response of the low ionosphere to X-ray and Lyman- $\alpha$  solar flare emissions. *J. Geophys. Res. Space Phys.* **2013**, *118*, 570–575. [[CrossRef](#)]
42. Taylor, J.R. *An Introduction to Error Analysis: The Study of Uncertainties in Physical Measurements*; University Science Books: Sausalito, CA, USA, 1997; pp. 181–198.
43. Goody, R.; West, R.; Chen, L.; Crisp, D. The correlated-k method for radiation calculations in nonhomogeneous atmospheres. *J. Quant. Spectrosc. Radiat. Transfer.* **1989**, *42*, 539–550. [[CrossRef](#)]
44. Zhang, Y.; Li, X.; Bai, Y. An integrated approach to estimate shortwave solar radiation on clear-sky days in rugged terrain using MODIS atmospheric products. *Sol. Energy* **2015**, *113*, 347–357. [[CrossRef](#)]
45. Curto, J.J. Geomagnetic solar flare effects: A review. *J. Space Weather Space Clim.* **2020**, *10*, 27. [[CrossRef](#)]
46. Kumar, A.; Kumar, S. Solar flare effects on D-region ionosphere using VLF measurements during low- and high-solar activity phases of solar cycle 24. *Earth Planets Space.* **2018**, *70*, 29. [[CrossRef](#)]

**Disclaimer/Publisher's Note:** The statements, opinions and data contained in all publications are solely those of the individual author(s) and contributor(s) and not of MDPI and/or the editor(s). MDPI and/or the editor(s) disclaim responsibility for any injury to people or property resulting from any ideas, methods, instructions or products referred to in the content.